Decontamination of Wind Measurements from Buoys Subject to Motions in a Seaway

J. P. DUGAN, S. L. PANICHAS AND R. L. DIMARCO

Areté Associates, Arlington, Virginia

(Manuscript received 26 September 1989, in final form 25 June 1990)

ABSTRACT

The motions of buoys in a seaway produce velocities at onboard anemometers that contaminate the measurements of wind, which typically is a severe problem for small, easily deployable buoys. The severity of this problem is quantified for a MINIMET buoy having a Gill and a propeller/vane anemometer at 3-m height, and a decontamination algorithm is derived and used to correct the Gill wind data. The model for the motions of the anemometer utilizes measurements of all six components of motion of the buoy. A gimballed compass is used to measure the yaw; a vertically stabilized platform measures heave, pitch, and roll; and horizontal linear accelerometers are used for surge and sway. The buoy surge and pitch produce the worst wind speed errors when the waves are in line with the wind. Of these two, the errors produced by the surge motions are larger for the case considered in detail here. The 3D velocity vector at the anemometer location as calculated from the motion measurements is coherently subtracted from the measured wind vector in the anemometer coordinate frame, and the result is transformed back to earth coordinates. The motion subtraction significantly affects the measured wind in a frequency band from roughly 0.1 to 0.6 Hz. The corrected wind fluctuations agree in general form with other measurements in a wind/wave tank and from a tower.

1. Introduction

The relationship of the wind and its fluctuations in the vicinity of the sea surface in the presence of waves is important for many air–sea interaction problems, including remote sensing of the surface for estimating wind speed and sea state (cf. Vesecky and Stewart 1982; Jones et al. 1982; Plant et al. 1983). However, good measurements of the wind and the waves are difficult to make inexpensively if one is interested in any details of the fluctuations. These measurements are routinely made in specific experiments from towers such as in JONSWAP (Hasselmann et al. 1973). Unfortunately, these stable platforms are not available in the deep sea, except for very large spar buoys such as FLIP (Fisher and Spiess 1963) and the Bouée Laboratoire, and they are not available at low cost. Smaller, unmanned buoys typically are used for wind and wave measurements because of their portability and low cost, but they suffer the disadvantage of exposing the anemometers to large motions due to surface waves. This is detrimental since these anemometer motions contaminate the detailed fluctuations in the wind (Pond 1968; Augstein and Wuchnitz 1969), and they even can affect the mean speed due to nonlinear rectification (Wyngaard 1981). This latter problem can be alleviated by using anemometers having rapid response, but the wave-induced motions of the sensor must be expected to dominate the smaller scale and higher frequency structure of the wind fluctuations. Attempts have been made to reduce the sensor motions by using unmanned spar buoys (e.g., Oregon State University TOTEM or Woods Hole Oceanographic Institution SPAR, Berteaux, 1976), but detailed analyses of their success are not available. Unfortunately, spars must be relatively long to decouple the surface motions (Tucker 1982) and they are not easily launched and retrieved.

A more easily deployable surface-following buoy has been constructed and tested that is intended to provide the wind and buoy motion data in a form that permits the motions to be accounted for. Engineering details of the buoy and the experience of its use at sea are provided by Dugan et al. (1989). Briefly, the test platform is a modified MINIMET buoy that has two anemometers and a complete motion measurement package. The primary anemometer is a UVW Gill meter, which is a reasonable compromise between rapid response and ruggedness in unattended operation (cf. Busch et al. 1980, and other chapters in the same monograph). A secondary anemometer is a propeller/vane meter. Both are standard instruments available from R. M. Young. The anemometers are mounted on a mast at 3-m height above the buoy hull, which is roughly a 1-m diameter sphere. The mast is held upright by the righting moment of weights hung from a bottom-mounted stem. The motions of the buoy are measured by a suite of three sensor packages mounted within the hull. A Syntron compass provides the yaw, a Datawell Hippy sensor measures the heave, roll, and pitch, and two Setra accelerometers yield the horizontal linear

Corresponding author address: Dr. J. P. Dugan, Arete Associates, P.O. Box 16287, Arlington, VA 22215-1287.

motions of the hull. These provide the required six degrees of freedom to which the buoy is exposed, but they do not measure them independently. In particular, the compass and the Datawell sensor are vertically oriented by their design, but the accelerometers are strapped to the hull. The latter sensors, therefore, respond not only to horizontal accelerations but also to tilts; i.e., pitch and roll, in the gravity field.

Figure 1 is a photograph of this buoy illustrating typical motion in a moderate seaway, sea state 4 on the Beaufort scale. The obvious tilt of the mast from the vertical clearly affects the wind measurements in several ways. The motion causing the tilt provides horizontal movement of the anemometer, so that the measured relative wind is different from the wind in the earth's coordinate system. In addition, the pitching motion in particular provides a rotary velocity about the center of mass. Finally, since the anemometer is at

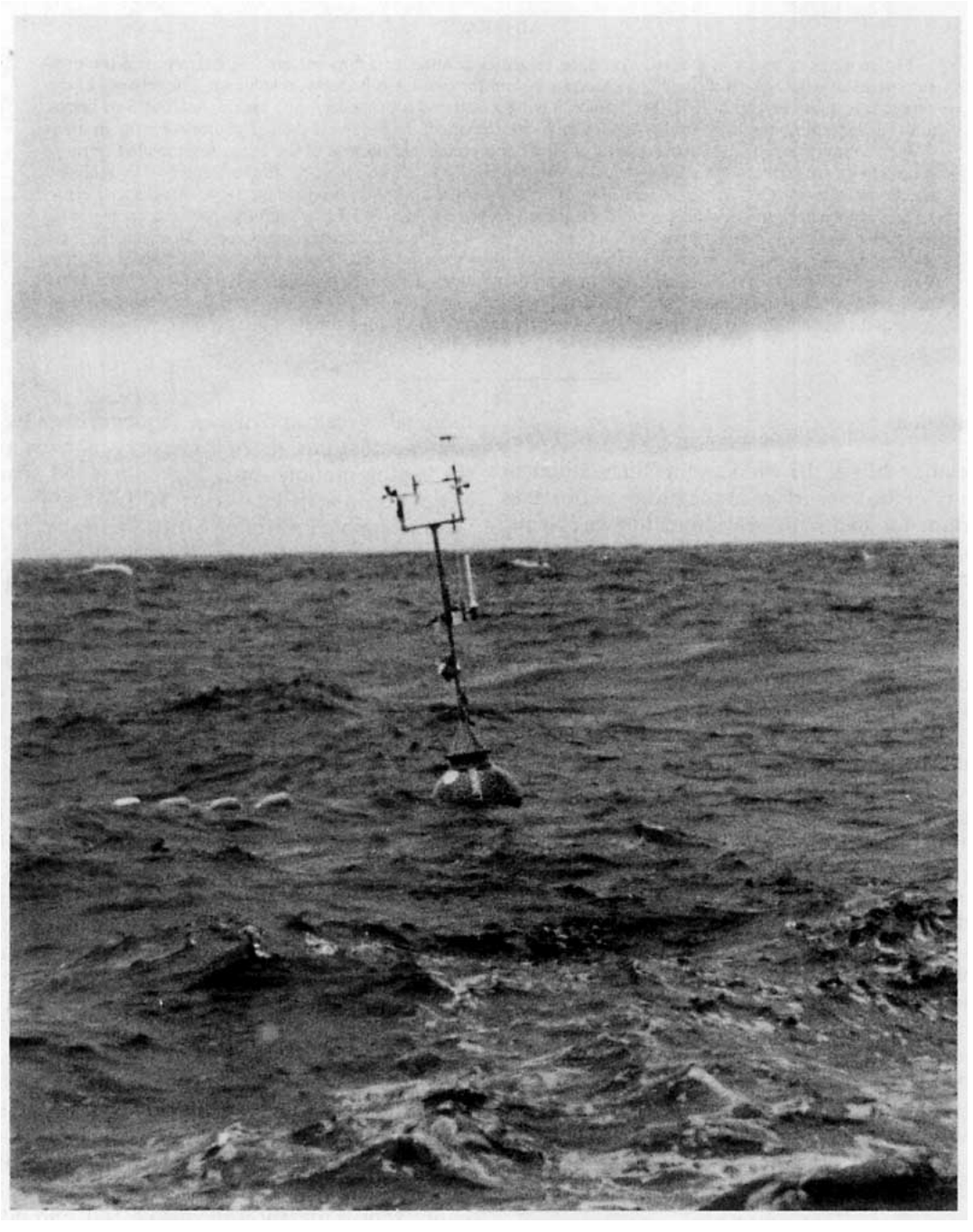

FIG. 1. Photo of MINIMET buoy exhibiting typical tilting motion in a sea state of 4 on the Beaufort scale.

an angle to the vertical, during the pitching motion, the horizontal arms measure only components of the true relative wind. The propeller/vane meter cannot measure this relative vertical component and, in addition, has finite azimuthal inertia so that it has a tendency to swing significantly further than the actual azimuthal angle of the wind during the tilting motion.

Figure 2 is a plot of the calculated motions of the Gill anemometer. The details of the calculation will unfold later but, for the moment, the two panels give an example of a few cycles of the motion in the forward/vertical plane in panel a and in the horizontal plane in panel b. The plots are phase diagrams with the axes in units of velocity. These data were collected when the mean wind speed was about 7 m s^{-1}, so the anemometer motions represent a significant fraction of the speed to be measured. Figure 2a exhibits the expected circular motions of a wave-following buoy for waves at small angles to the x axis. This is corroborated in Fig. 2b where the range of velocities in the x direction are twice those in the y direction.

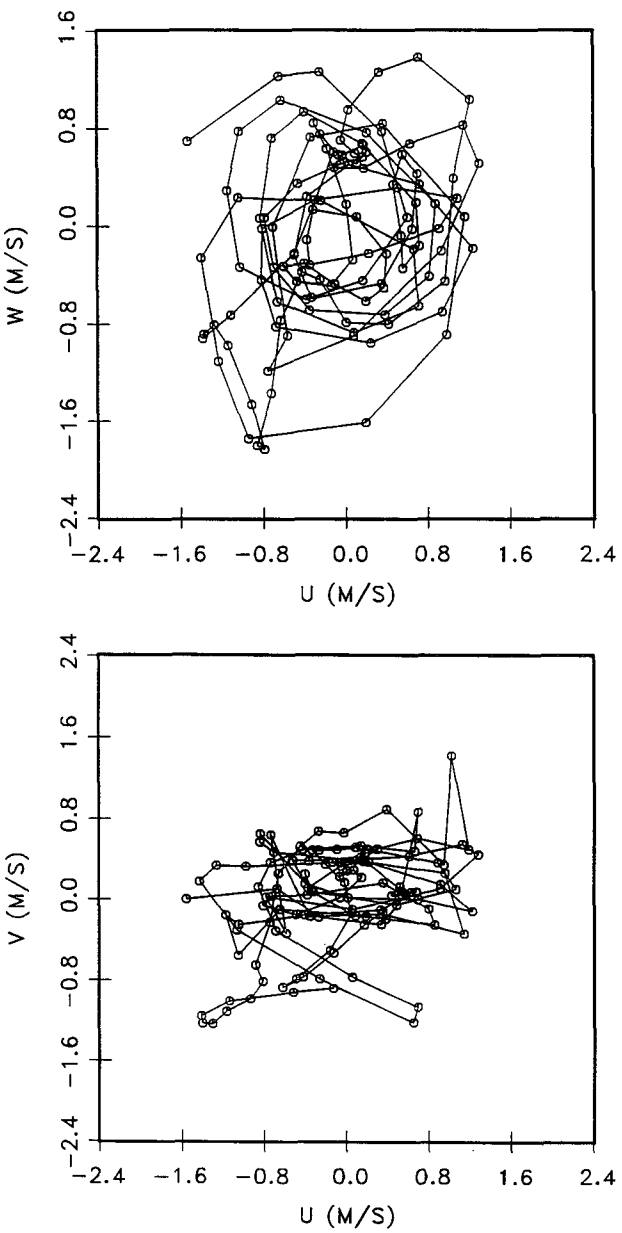

FIG. 2. Phase plots of anemometer motions in the forward-vertical plane (a) and the horizontal plane (b), containing 30 s of 4-Hz data.

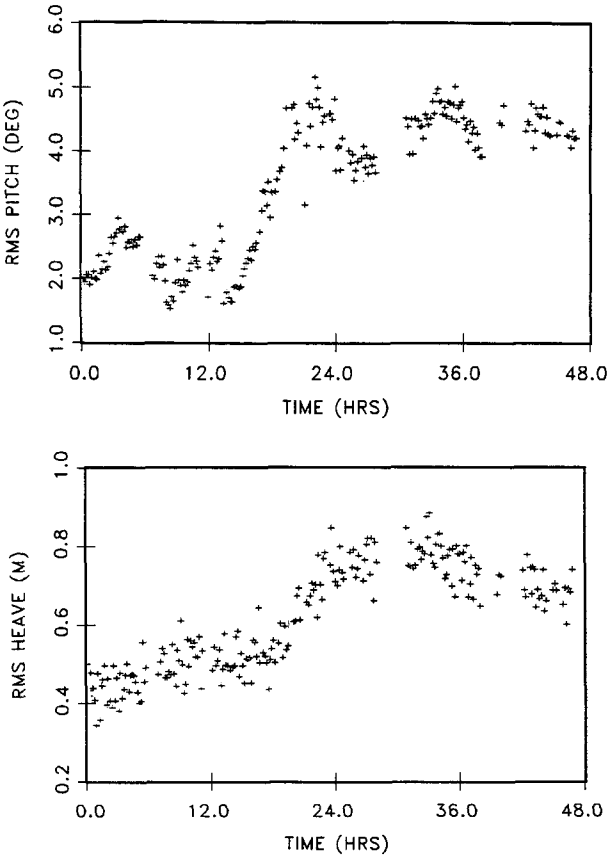

FIG. 3. Time series of rms pitch (a) and rms heave (b) over a 48-h period. The rms values are calculated on 1-min intervals, which accounts for the noisy time series.

For this buoy, the roll and pitch clearly are motions that cause errors in the wind measurements. The pitch most directly enters speed measurements and the roll affects the direction, in the typical situation in which the buoy is roughly pointed into both the wind and the waves. Thus, a simple measure of the performance in terms of the verticality of the buoy is the rms pitch. Figure 3 shows an example of the 1-min rms pitch and heave for 48 h of data. The sea state changes by a factor of two during this period, as evidenced by the rms heave. Evidently, the degree of tilting motion is a function of the sea state, so one expects that the anemometer errors will increase with an increase in the wave amplitude. The spectrum of pitch data is shown

in Fig. 4a. The peak below 0.2 Hz is the natural frequency of the pendulum motion of the buoy/weight system, and the peak near 0.47 Hz indicates the natural frequency of tilting motions of the buoy, as shown by Dugan et al. (1989). Figure 4b is the concomitant heave spectrum showing the swell peak at 0.1 Hz and the natural frequency of heave motions at 0.60 Hz. For these specific data, the mean wind speed is 7 m s^{-1}, so the corresponding fully developed wind–wave spectrum has a peak at about 0.22 Hz, as shown by the vertical line at the frequency axis. The spectral slope of the higher frequency wind–wave motions clearly is very near the accepted −4 power law. Finally, Fig. 4c is the coherence between the pitch and heave, and the magnitude is consistently high all across the wind–wave and swell band. The two motions are nearly 180° out of phase for the swell, and they change to about −90° (i.e., heave leads pitch by about 90°) for the wind waves and the buoy resonance frequency.

The purpose of this paper is to provide to the oceanographic community the procedures that are used to decontaminate the wind data, and to document the results that have been attained. Section 2 describes the algorithm that has been derived for calculating the motions of the anemometers, and section 3 provides the results of its application to actual data.

2. Analysis procedure

Motion of the buoy can be completely described by the three-dimensional translational motion of a reference point on the buoy, and three rotations about that point. The reference point used is the center of the buoy sphere, which will be subsequently referred to as the center of mass (CM). Since all six components of the rigid body motion are specified it does not matter if this point is the true center of mass of the system. In the following, quantities derived from buoy rotations will be denoted by the subscript rot, (i.e., the acceleration of the instrument due solely to rotations is a_{rot}). Three angles are measured to specify the rotation of the buoy, these are the pitch (P), roll (R) and yaw (Y) as shown in the upper part of Fig. 5. In the figure the primed axes represent the buoy coordinate system (hereafter CS), while the unprimed axes represent the earth CS. The pitch and roll are the forward and starboard tilts of the buoy with respect to a gravity stabilized platform. The yaw is provided by a gimballed compass. As defined these three angles are not independent and so are not suitable for coordinate transformations. They may be combined to form the Eulerian angles, Θ, Ψ, and Φ, which are independent, as follows:

$$\Theta = \sin^{-1}(\sin^2 P + \sin^2 R)^{1/2} \quad (1)$$

$$\Psi = \tan^{-1}(\sin P/\sin R) \quad (2)$$

$$\Phi = Y - \tan^{-1}(\tan\Psi \cos\Theta). \quad (3)$$

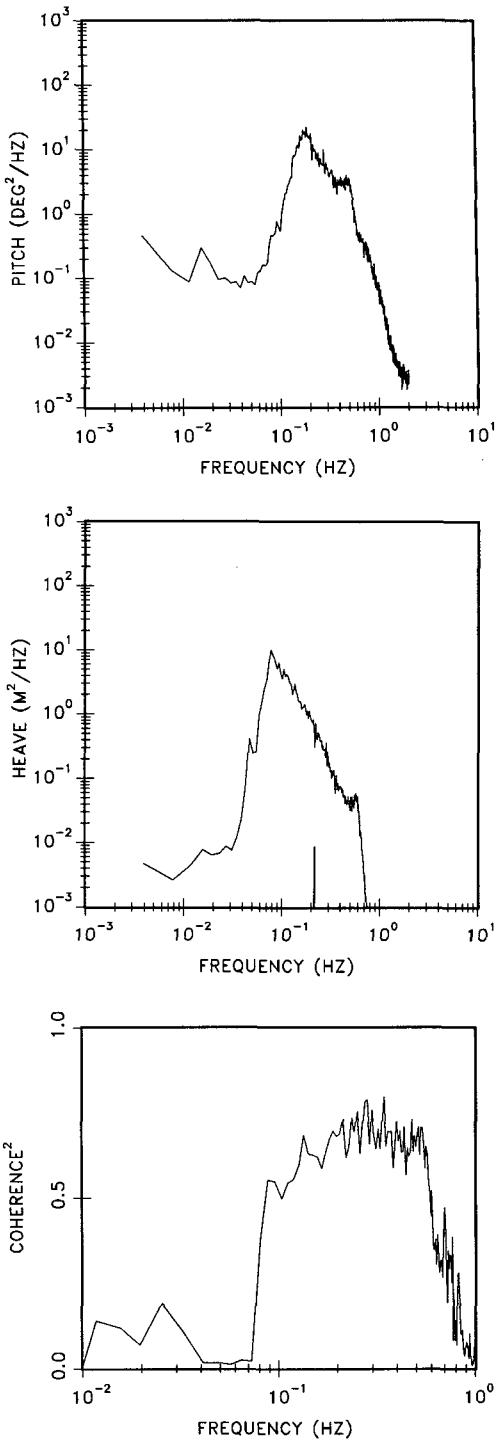

FIG. 4. The spectra of the tilting motions (pitch) (a) and heave motions (b) and the squared coherence between them (c) for 2.5 h of data from the end of the time period presented in Fig. 3.

These angles are shown in the lower part of Fig. 5. In the construction of the buoys, the x–y axes of the Datawell Hippy sensors, which measure P and R, were

not aligned with the defined buoy x–y axes. In our two buoys the axes were rotated counterclockwise by 6° and 16°. This rotation can be removed by subtracting the offset angle, κ, from the Euler angle Ψ', as defined in Eq. 2:

$$\Psi = \Psi' - \kappa. \tag{4}$$

The set of Euler angles, θ, Ψ, and Φ, are independent and so may be used to generate transformation matrices between the buoy and earth coordinate systems, as well as the angular velocity vector for rotations about the buoy center of mass. The angles chosen are the same as used by Goldstein (1965), and so his results for these quantities will be used. The matrix used to transform vectors from buoy to earth coordinates is

$$\mathbf{T}_{BE} = \begin{pmatrix} \cos\Psi\cos\Phi - \cos\theta\sin\Phi\sin\Psi & -\sin\Psi\cos\Phi - \cos\theta\sin\Phi\cos\Psi & \sin\theta\sin\Phi \\ \cos\Psi\sin\Phi - \cos\theta\cos\Phi\sin\Psi & -\sin\Psi\sin\Phi + \cos\theta\cos\Phi\cos\Psi & -\sin\theta\cos\Phi \\ \sin\theta\sin\Psi & \sin\theta\cos\Psi & \cos\theta \end{pmatrix}. \tag{5}$$

The matrix for the reverse transfer is given by

$$\mathbf{T}_{EB} = \begin{pmatrix} \cos\Psi\cos\Phi - \cos\theta\sin\Phi\sin\Psi & \cos\Psi\sin\Phi + \cos\theta\cos\Phi\sin\Psi & \sin\Psi\sin\theta \\ -\sin\Psi\cos\Phi - \cos\theta\sin\Phi\cos\Psi & -\sin\Psi\sin\Phi + \cos\theta\cos\Phi\cos\Psi & \cos\Psi\sin\theta \\ \sin\theta\sin\Phi & -\sin\theta\cos\Phi & \cos\theta \end{pmatrix}. \tag{6}$$

In the earth CS the angular momentum vector is given by

$$\omega = \begin{bmatrix} (\dot\theta\cos\Phi + \dot\Psi\sin\theta\sin\Phi)\hat i \\ (\dot\theta\sin\Phi - \dot\Psi\sin\theta\cos\Phi)\hat j \\ (\dot\Psi\cos\theta + \dot\Phi)\hat k \end{bmatrix}. \tag{7}$$

At any time point, each of these quantities is defined by the instantaneous value of θ, Φ, and Ψ, and their derivatives.

Translational motion of the buoy center of mass, denoted throughout by the subscript mot, are measured by linear accelerometers. Two of these instruments are aligned with the buoy x and y axes, but not on the centerline of the buoy as shown schematically in Fig. 6. The third accelerometer is on a gravity stabilized platform (cf. Brainard and Gardiner 1982) and so measures the z component of motion in earth system. These three measurements, while not independent, can be combined using the transformation matrices to specify the 3-component linear acceleration in either the buoy or earth CS.

The wind is measured in a third coordinate system, referred to as the Gill CS. This system has its z axis parallel to the buoy CS, and its x and y axes rotated by 45° about z as shown in Fig. 6. Thus, transformations from the buoy to Gill CS are simple rotations about the z axis. This configuration prevents either of the horizontal propellers from being a stall region when the wind comes from the front of the buoy (x axis) as was typical. In the present notation, parameters in the earth CS are unprimed, in the buoy CS they are primed and in the Gill CS they are double primed.

The motion of the anemometer is a sum of the rectilinear motions of the buoy CM plus rotations—that is tilting motions—about the CM. The processing used to extract these motions from the data is summarized in the block diagram shown in Fig. 7. The rectilinear motion can be extracted from the accelerometer data, with corrections of the horizontal data for the tilts in the gravity field and of all components for noncoincidence of CM and the sensors. The rotational acceleration is given by the expression

$$\mathbf{a}_{\text{mot}} = \omega \times (\omega \times \mathbf{r}) + \left(\frac{d\omega}{dt} \times \mathbf{r}\right) \tag{8}$$

where $\mathbf{r}$ is the distance vector from the buoy center of mass to the individual accelerometer positions; ω is the angular velocity vector about the center of mass as described by the Euler angles. The quantity ω is expressed in the buoy cs for the two horizontal accelerometers and in the earth cs for the vertical accelerometer. Horizontal CM acceleration in the buoy cs is described by

$$a'_{x_{\text{cm}}} = a'_{x_{\text{meas}}} - a'_{x_{\text{mot}}} + g\sin P' \tag{9}$$

$$a'_{y_{\text{cm}}} = a'_{y_{\text{meas}}} - a'_{y_{\text{mot}}} - g\sin R' \tag{10}$$

where

$$P' = -P_{\text{meas}}\cos\kappa + R_{\text{meas}}\sin\kappa$$

$$R' = -P_{\text{meas}}\sin\kappa + R_{\text{meas}}\cos\kappa. \tag{11}$$

P' and R' are the effective pitch and roll along the buoy x and y axes. The sign of the gravity tilt term is positive in (9) due to the definition of positive pitch.

Vertical acceleration in the earth CS is given by

$$a_{z_{\text{cm}}} = a_{z_{\text{meas}}} - a_{z_{\text{rot}}}. \tag{12}$$

Using the known values of $a'_{x_{\text{cm}}}$, $a'_{y_{\text{cm}}}$, and $a_{z_{\text{cm}}}$, and the earth to buoy transformation matrix, $\mathbf{T}_{EB}(\theta, \Psi, \Phi)$, one can solve two simultaneous equations for $a_{x_{\text{cm}}}$ and $a_{y_{\text{cm}}}$ (earth CS) and then determine $a'_{z_{\text{cm}}}$. Dropping the subscript cm, one obtains

$$a'_x = \mathbf{T}_{EB}(1,1)a_x + \mathbf{T}_{EB}(1,2)a_y + \mathbf{T}_{EB}(1,3)a_z \tag{13}$$

$$a'_y = \mathbf{T}_{EB}(2,1)a_x + \mathbf{T}_{EB}(2,2)a_y + \mathbf{T}_{EB}(2,3)a_z. \tag{14}$$

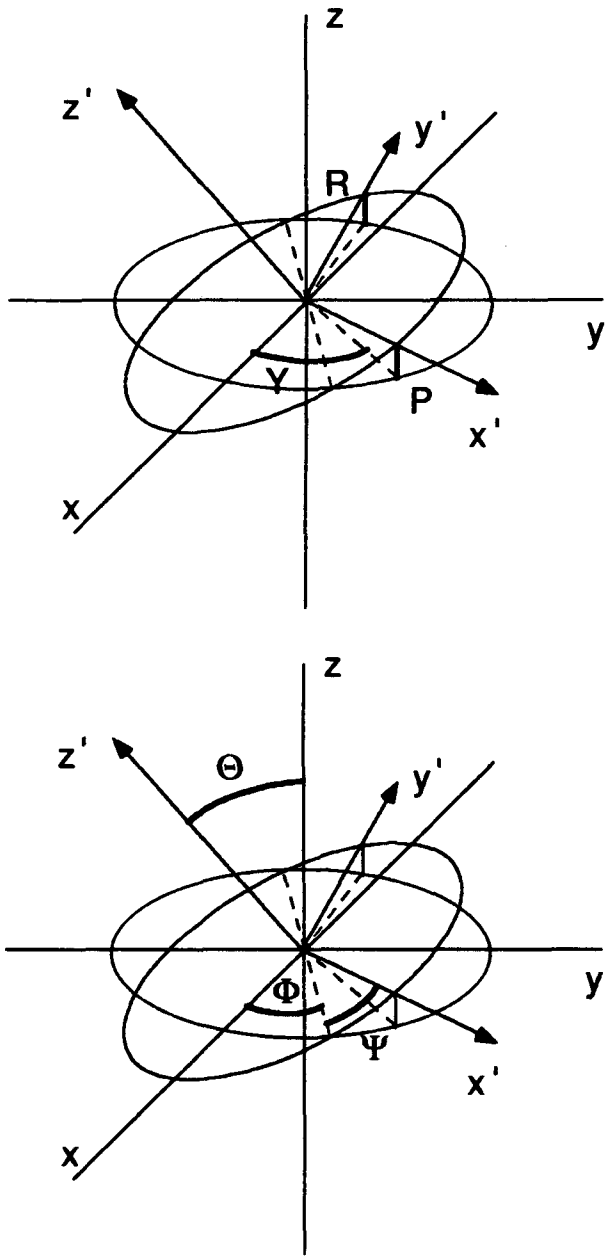

FIG. 5. Earth and buoy (primed) coordinate systems showing (a) the measured angles: pitch (P), roll (R), and yaw (Y) and (b) the Euler angles used for coordinates transformations

After solving for a_x and a_y, a'_z can be determined:

$$a'_z = \mathbf{T}_{EB}(3, 1)a_x + \mathbf{T}_{EB}(3, 2)a_y + \mathbf{T}_{EB}(3, 3)a_z. \quad (15)$$

Now that all three CM accelerations are expressed in the buoy CS, they can be integrated to get CM velocities. In processing the data, however, low frequency noise from the periodic transmitter on/off cycle was noted as a peak in the power spectrum at 60 s, with a second peak at 30 s, its first harmonic. This noise was most evident in the accelerometer data, presumably due to their low signal levels and less than optimal gain (Dugan et al. 1989). To prevent this low frequency noise from contaminating the integration, the accelerometer data were first high-pass filtered at a rollover period of 20 s, and then integrated numerically using a 5-point Simpson's rule:

$$\mathbf{v}'_{cm} = \int \mathbf{a}'_{cm}\, dt. \quad (16)$$

At this stage, the rigid body CM velocity of the buoy and hence of the anemometers is calculated in three dimensions.

The wind measured at the Gill anemometer is a sum of the true wind and the velocity generated by the motion of the buoy. This motion velocity is a sum of the CM buoy velocity described by (16), and the velocity due to the anemometers not being at the center of mass on the tilting buoy—a rotational velocity described by

$$\mathbf{v}'_{i_{rot}} = \omega \times \mathbf{r}_i; \quad i = 1, 2, 3 \quad (17)$$

where i indicates the three Gill propellers, and $\mathbf{r}_i$ is the distance vector from the center of mass to each propeller. For each Gill propeller, the motion velocity in the buoy CS is given by

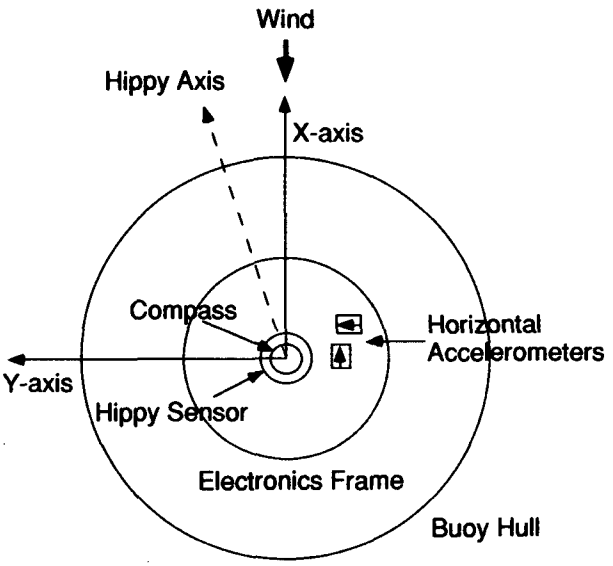

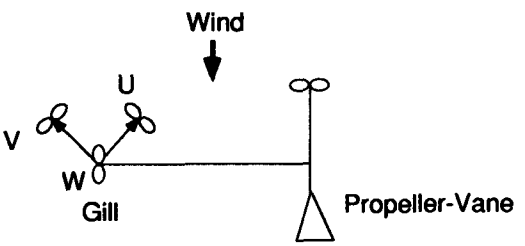

FIG. 6. Diagram of the locations of the motion sensors within the buoy hull.

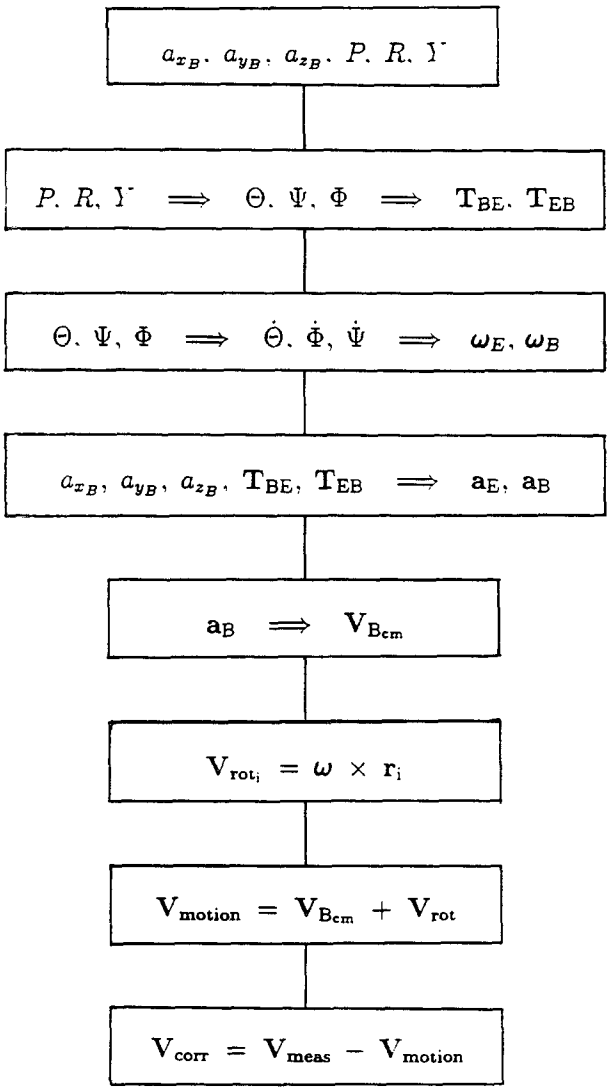

FIG. 7. Block diagram of the motion decontamination procedures.

$$\mathbf{v}'_{mot} = \mathbf{v}'_{cm} + \mathbf{v}'_{rot}. \tag{18}$$

Since the wind measurements are made in the Gill CS, the motion velocities must be transformed from the buoy CS to the Gill CS before they can be subtracted from the measured winds:

$$\mathbf{v}''_{mot} = \mathbf{T}_{BG}\mathbf{v}'_{mot} \tag{19}$$

and

$$\mathbf{v}''_c = \mathbf{v}''_{meas} - \mathbf{v}''_{mot}. \tag{20}$$

Here, $\mathbf{v}''_c$ is the corrected wind for each component of the three Gill propellers. One aspect of the Gill anemometer is that the propellers react to wind from all angles except 90° to the anemometer axes. The slight noncosine response of these propellers is accounted for through an iterative process that uses all three measured wind components to determine the wind speed along each of the measurement axes as in Horst (1972, 1973); correction factors for additional propeller types are given in Bowen and Teunisson (1986). Propeller stall has been observed on the vertical component, and this only at very low wind speed, but no attempt has been made to cast all axes to the mean wind direction as done by Atakturk and Katsaros (1989) or Horst (1973).

The last step in the motion decontamination process is to transform the three wind components to the earth cs and, then, to combine them into wind speed and direction:

$$\mathbf{v}'_c = \mathbf{T}_{GB}\mathbf{v}''_c$$
$$\mathbf{v}_c = \mathbf{T}_{BE}\mathbf{v}'_c. \tag{21}$$

Here,

$$\text{horizontal wind speed} = (v_{c_x}^2 + v_{c_y}^2)^{1/2};$$
$$\text{Horizontal wind direction} = \tan^{-1}(v_{c_y}/v_{c_x});$$
$$\text{Vertical wind speed} = v_{c_x}. \tag{22}$$

3. Results

The buoy motion algorithm discussed in the foregoing has been used to decontaminate wind speed measurements from the Gill anemometer. Figure 8 is a spectral plot of the speed of the anemometer mounting for a case in which the rms wave height was 0.7 m and the mean wind speed was 7 m s^{-1}. These data, as well as other data shown in this paper, were recorded

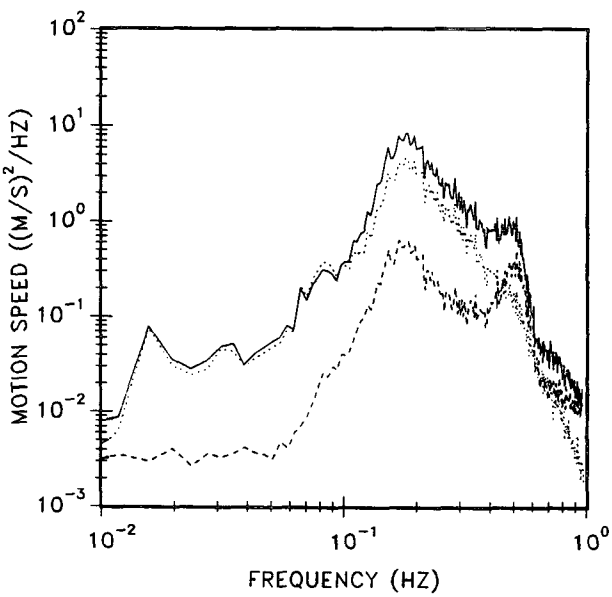

FIG. 8. Spectra of the motions of the anemometer in the forward direction: total motion (solid line), rectilinear motion (dotted line), and rotational motion (dashed line).

in October off the coast of southern California, in open water. The solid line is the spectrum of the calculated total speed of the anemometer mounting, which later will be subtracted from the wind speed measurement. It has peaks at both the pendulum resonance frequency and the buoy pitch resonance frequency. The much smaller peak at $^1/_{60}$ Hz is due to contamination caused by the transmitter as mentioned previously, and it is of no consequence in the following. The dotted line is the portion of the spectrum due to translational motion, and the dashed line is the portion due to tilting motion. Clearly, the linear accelerations are the major source of contamination except near the pitch resonance frequency of the buoy. This result is in general accord with measurements from a different type of buoy discussed by Augstein and Wucknitz (1969), although they have provided much less detail.

Figure 9a is the spectrum of wind speed as measured by the Gill anemometer compared with the total anemometer motion exhibited in the previous figure. As before, the mean wind speed was 7 m s^{-1}. For this combination of wind speed (and, therefore, wind fluctuation level) and wave height, the motion of the buoy contaminates the wind measurements at frequencies above about 0.15 Hz. As expected from the close agreement in spectral level between the two quantities, the coherence between them is high, and this is presented in Fig. 9b. For comparison, the coherence between measured wind speed and vertical heave is also shown in Fig. 9b.

The spectrum of the corrected wind speed is shown in Fig. 10a, along with the spectrum of measured wind that was presented in Fig. 9a. The motion correction process clearly decreases the energy in the wind wave band by a factor of 3 or so. More striking evidence of the success of the motion decontamination process is provided in Fig. 10b, which presents the squared coherence between the corrected wind speed and anemometer motion speed, and the squared coherence between the measured wind and motion speed as shown in Fig. 9b. The dotted line in this figure is the squared coherence between the corrected wind speed and the heave channel. The motion removal algorithm reduces the squared coherence between anemometer motion and wind speed from 0.8 to 0.1 at the tilt resonance frequency near 0.5 Hz. The reduction in coherence is less than this across the rest of the frequency band of buoy motion, but the difference is significant. A comparison of the level of coherence between heave and the wind speeds, the lowest lines in Figs. 9b and 10b, indicate a reduction from 0.55 for the measured wind to about 0.3 for corrected wind in the swell band. The residual coherence between corrected wind and heave is a combination of errors in the decontamination process and the wave-induced wind fluctuations that occur naturally.

A simple empirical measure of the wave-induced wind fluctuations may be determined by calculating

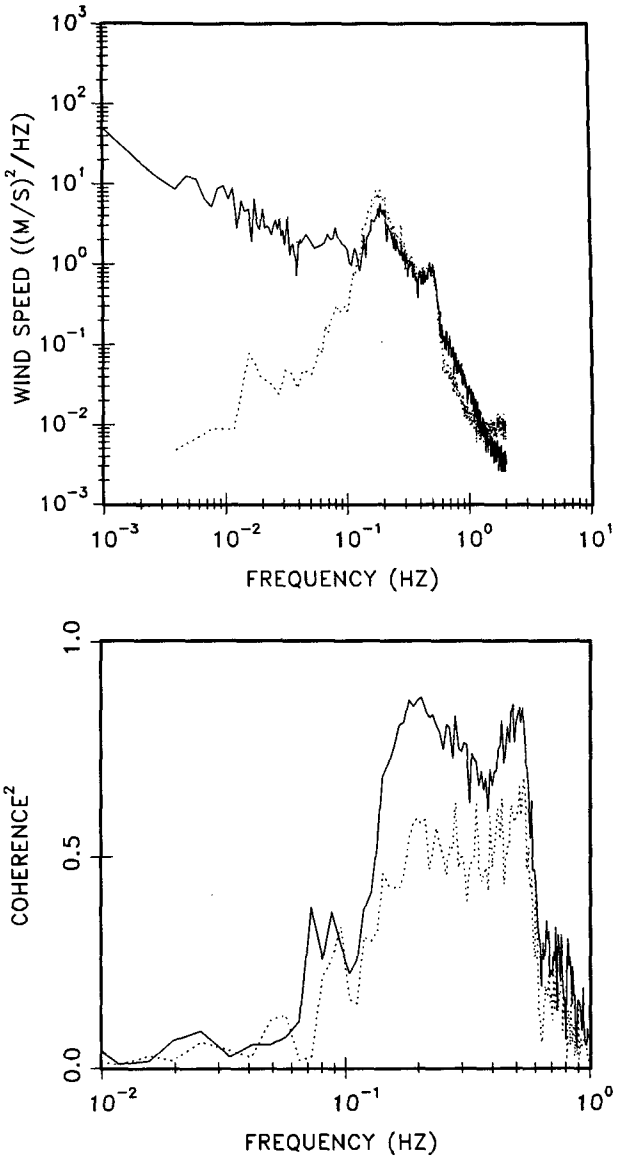

FIG. 9. Spectra of measured wind speed (solid line) and total anemometer motion (dotted; also solid line in Fig. 7) (a) the squared coherence between measured wind and anemometer motion velocity (solid line) and between measured wind and heave (dotted line) (b). Mean wind speed was 7 m s^{-1} and rms heave was 7.0 m.

the potential flow generated by the presence of the waves. For this calculation, a zero mean wind has been assumed, the heave spectrum as the wave-height spectrum, $\mathbf{S}_\eta(\omega)$ was used, and the formulation of Kitaigorodskii (1970) has been adapted to obtain the following expression for wind fluctuations associated with potential flow at the air–sea interface:

$$\mathbf{S}_u(\omega) = \mathbf{S}_\eta(\omega)\omega^2 e^{-(2\omega^2 z/g)}, \qquad (23)$$

where $\mathbf{S}_u(\omega)$ is the spectrum of the orbital speed of the wind at height z. Application of this equation yields the potential flow fluctuation spectrum plotted in Fig.

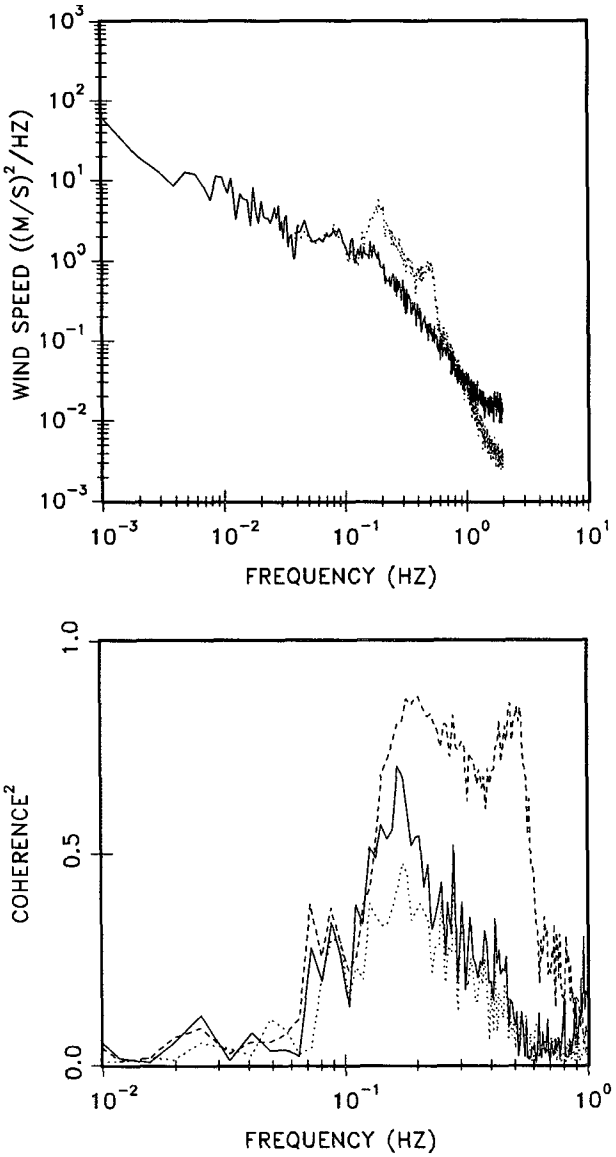

FIG. 10. Spectra of corrected wind speed (solid line) and measured wind (dotted line) (a) the squared coherence between corrected wind and the anemometer motion velocity (solid line), corrected wind and heave (dotted line); and measured wind and anemometer motion (dashed line) (b).

11 in comparison with the spectrum of the motion-corrected wind. Given the shape of the potential flow spectrum and its level in comparison with the wind spectrum, it is reasonable to expect the level of coherence of heave with corrected wind speed across the band 0.075 to 0.2 Hz to be fairly constant at some significantly nonzero level. Figure 10b indicates this level to be about 30% between corrected wind and heave for this particular case. Although there have been no measurements that compare directly with these data, the level is consistent with the provided results of Elliott (1972), Kondo (1972), and Haase et al. (1978). The spectral and coherence levels are unaffected by the motion removal process at frequencies below 0.1 Hz because the buoy motions do not contaminate the measurements at these lower frequencies. Thus, the coherence level of the longer swell and the wind ($\sim$0.3) seems to be a good measure of the real swell-induced wind fluctuations. Note, for instance, that the three coherence levels in Fig. 10 are the same for frequencies less than 0.1 Hz.

The real issue, then, is what portions of the higher coherence levels in the higher frequencies are due to remaining contamination. The coherence between corrected wind and heave is only slightly higher for frequencies between 0.1 and 0.2 Hz than it is below 0.1 Hz, and it is not clear that even this difference is significant. On the other hand, the level for the corrected wind with anemometer motion is significantly higher, and it is suspected that this is at least partially due to remaining contamination. Presently, it is not possible to distinguish between the two sources of energy, and to obtain a quantitative estimate of the performance of the algorithm, as a function of wind speed or, perhaps, other variables.

Since one cannot obtain a direct estimate of the residual contamination the following analysis was performed that yields a relative measure of the residual contamination as a function of wind speed. In this way one can determine where the correction procedure breaks down at low wind speed. A random sample of the collected data was polled, spanning the full range of wind speeds encountered, and variances were calculated over 30-min intervals in the frequency band of 0.15 to 0.3 Hz, since this is the band in question.

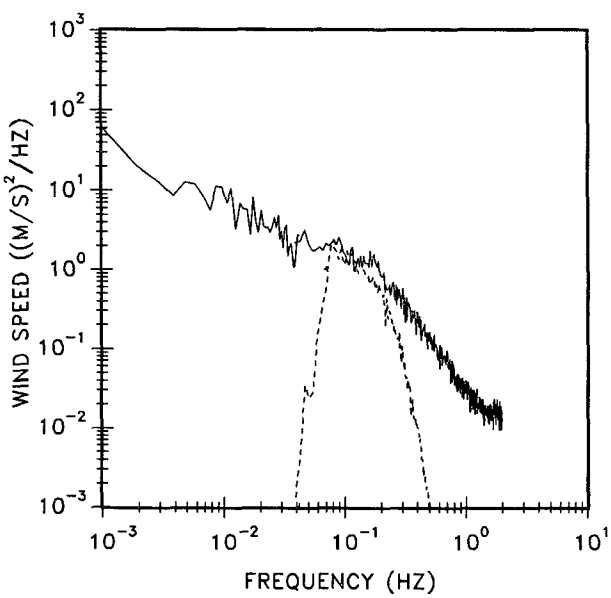

FIG. 11. Spectra of potential flow variance derived from heave channel (dashed line) and the corrected wind speed (solid line).

Most of the winds in the random sample were between 2 and 8 m s^{-1}, with only a few cases greater than 8 m s^{-1}. The measured wind speed is a sum of the true wind fluctuations (including wave-induced wind fluctuations), and the motion-induced fluctuations. The corrected wind speed is a sum of the true wind and the wave-induced wind fluctuations, and also some residual contribution from buoy motion since the removal process is imperfect. To get an estimate of the error, the sum of the corrected wind variance and anemometer motion variance is subtracted from the measured wind variance, and the ratio of this variance to the measured wind variance is presented in Fig. 12. If this difference were taken coherently the result would be zero, since this is how the corrected wind is determined. However, because in this case variances are subtracted rather than doing a point-by-point coherent subtraction, a quantity is obtained that, while not a direct measurement of the contamination, is expected to increase as the residual contamination increases. Above 3 m s^{-1}, this variance ratio has an average value of about 20%, whereas below 3 m s^{-1}, it increases markedly. Thus, for wind speeds less than 2–3 m s^{-1}, it would appear that the motion removal process performs poorly. It has been experienced, however, that the motion removal process performs reasonably well in light winds as long as the local sea is in equilibrium or underdeveloped with respect to the local wind (e.g., see the few data points in Fig. 12 where the ratio is small for low wind speed). If, however, the wind has decreased from some much higher value, and the waves are overdeveloped with respect to the local wind, then the buoy motions are relatively large compared with the wind speed fluctuations, and the motion removal algorithm does not perform as well. In either case, it is believed that motion removal will not be effective when performed on wind speeds less than about 2 m s^{-1} with this type of buoy. At the highest wind speeds observed in the data available for this study, 11 m s^{-1}, the variance ratio remains flat. Thus, the high-wind cutoff for this methodology is unknown while the low-wind cutoff is at wind speeds too small to be of interest for most practical applications.

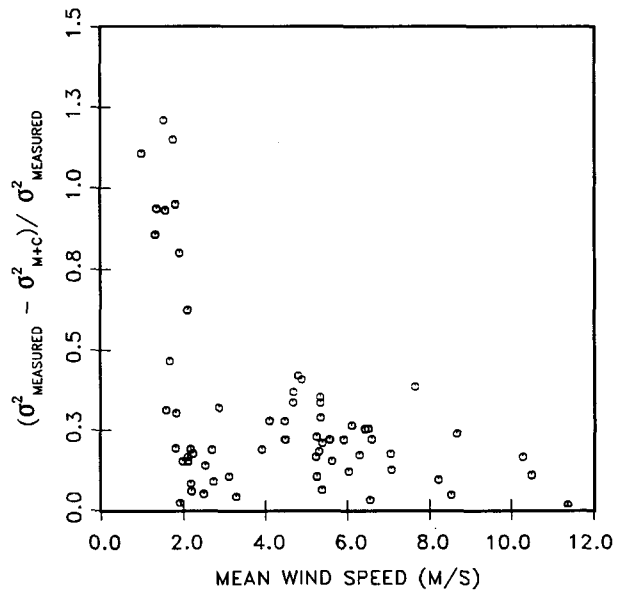

FIG. 12. Measure of residual variance in the corrected wind. Ratio of the difference between the sum of the motion and corrected wind variance (σ^2_{meas}) to the measured wind variance. Plotted versus wind speed.

4. Summary

Data from a MINIMET buoy have been analyzed for motions in a seaway. These motions have been shown to contaminate measurements of the wind and also measurements of the linear acceleration by the fixed accelerometers. The acceleration data, corrected for buoy tilt, indicate that the predominant motion affecting the wind measurements is rectilinear accelerations at frequencies less than the buoy heave and pitch resonant frequencies. Near these resonant frequencies, ~0.5 Hz, the tilting motion contamination is dominant. The measured wind is a combination of the true wind fluctuations, wave-induced wind fluctuations, and motion-induced wind fluctuations. An algorithm for removing the effects of motion from the wind measurements has been presented, and its application reduces the contamination considerably. A reduction in energy by a factor of three in the wind speed spectrum is observed in the wind–wave frequency band of 0.15–0.6 Hz for a case in which the wind is 7 m s^{-1} and the rms wave height is 0.7 m. A random sample of data encompassing wind speeds of 1–12 m s^{-1} indicates the motion-corrected wind has a residual variance that is a sum of the wave-induced wind fluctuations and residual buoy motions, and the residual is large for overdeveloped seas and/or wind speeds <2 m s^{-1}. Unfortunately, without an independent measure of the wind, there is no way of differentiating these two components, although a simple calculation of the energy of the wave-induced wind fluctuations using potential flow theory implies that most of the energy in the corrected wind spectrum in the wave band can be attributed to wave-induced fluctuations and not residual buoy motions.

REFERENCES

Atakturk, S., and K. B. Katsaros, 1989: The K-Gill: a twin propeller-vane anemometer for measurements of atmospheric turbulence. *J. Atmos. Oceanic Technol.*, **6**, 509–515.

Augstein, E., and J. Wucknitz, 1969: The quality of wind speed measurements on a semi-stabilized buoy, "*Meteor*" *Forschungsergeb.*, **3**, 28–32.

Berteaux, H. D., 1976: *Buoy Engineering.* J. Wiley, 314 pp.

Bowen, A. J., and H. W. Teunisson, 1986: Correction factors for the directional response of Gill propeller anemometers. *B-LM*, **37**, 407–413.

Brainard, E. C., and D. L. Gardiner, 1982: Wave-Track and Waverider

heave buoy intercomparisons at the entrance to the Columbia River. *Oceans,* **82,** 861–866.

Busch, N. E., O. Christensen, L. Kristensen, L. Lading and S. E. Larson, 1980: Cups, vanes, propellers and laser anemometers. *Air-Sea Interactions: Instruments and Methods,* F. Dobson, L. Hasse and R. Davis, Eds., Plenum, 11–46.

Dugan, J. P., S. L. Panichas, W. D. Morris and K. C. Vierra, 1989: Performance evaluation of the MINIMET air–sea interactions buoy. *Proc. MDS '89, Conf. and Exposition on Marine Data Systems,* Marine Technology Society, New Orleans, 250 pp.

Elliot, J. A., 1972: Microscale pressure fluctuations near waves being generated by the wind. *J. Fluid Mech.,* **54,** 427–448.

Fisher, F. H., and F. N. Spiess, 1963: FLIP—floating instrument platform. *J. Acoust. Soc. Amer.,* **35,** 1633–1644.

Goldstein, H., 1965: *Classical Mechanics.* Addison-Wesley, 399 pp.

Haase, L., M. Greenewald and D. E. Hasselmann, 1978: Field observations of air flow above the waves. *Turbulent Fluxes through the sea surface, wave dynamics, and prediction,* A. Faure and K. Hasselman, Eds., Plenum, 483–494.

Hasselmann, K., T. P. Barnett, E. Bouws, H. Carlson, D. E. Cartwright, K. Enke, J. A. Ewing, H. Gienapp, D. E. Hasselmann, P. Kruseman, A. Meerburg, P. Muller, D. J. Olbers, K. Richter, W. Sell and H. Walden, 1973: Measurement of wind–wave growth and swell decay during the Joint North Sea Wave Project (JONSWAP). *Dtsch. Hydrogr. Z.,* **12,** 1–95.

Horst, T. W., 1972: A computer algorithm for correcting noncosine response in the Gill anemometer. Batelle Pacific Northwest Lab Rept BNWL-1651-1, 183–186.

——, 1973: Corrections for response errors in a three component propeller anemometer. *J. Appl. Meteorol.,* **12,** 716–725.

Jones, W. L., L. C. Schroeder, D. Boggs, E. M. Bracalente, R. A. Brown, G. Dome, W. J. Pierson and F. J. Wentz, 1982: A Seasat-A satellite scatterometer: the geophysical evaluation of remotely sensed wind vectors over the ocean. *J. Geophys. Res.,* **87,** 3297–3317.

Kitaigorodskii, S. A., 1973: *The Physics of Air-Sea Interaction.* Israel Programme for Scientific Translations, 237 pp.

Kondo, J., Y. Fujinawa and G. Naito, 1972: Wave-induced wind fluctuations over the sea. *J. Fluid Mech.,* **51,** 751–771.

Plant, W. J., W. C. Keller and A. Cross, 1983: Parametric dependence of ocean wave-radar modulation transfer function. *J. Geophys. Res.,* **88,** 9747–9756.

Pond, S., 1968: Some effects of buoy motion on measurements of wind speed and stress. *J. Geophys. Res.,* **73,** 507–512.

Tucker, M. J., 1982: The heave response of a spar buoy. *Ocean Eng.,* **9,** 259–270.

Vesecky, J. F., and R. H. Stewart, 1982: The observation of ocean surface phenomena using imagery from the Seasat synthetic aperture radar: an assessment. *J. Geophys. Res.,* **87,** 3397–3430.

Wyngaard, J. C., 1981: Cup, propeller, vane and sonic anemometers in turbulence research. *Ann. Rev. Fluid Mech.,* **13,** 399–423.